








Computed Tomography Imaging for Monitoring of Marburg Virus Disease: a Nonhuman Primate Proof-Of-Concept Study

Jennifer Sword,^{a*} Ji Hyun Lee,^{a§}  Marcelo A. Castro,^a Jeffrey Solomon,^b Nina Aiosa,^{a◇} Syed M. S. Reza,^c  Winston T. Chu,^c Joshua C. Johnson,^{a∞} Christopher Bartos,^a Kurt Cooper,^a Peter B. Jahrling,^{a,d‡} Reed F. Johnson,^{a,d#} Claudia Calcagno,^a  Ian Crozier,^b  Jens H. Kuhn,^a Lisa E. Hensley,^{a¶} Irwin M. Feuerstein,^{a**}  Venkatesh Mani^a

^aIntegrated Research Facility at Fort Detrick, Division of Clinical Research, National Institute of Allergy and Infectious Diseases, Fort Detrick, National Institutes of Health, Fort Detrick Frederick, Maryland, USA

^bClinical Monitoring Research Program Directorate, Frederick National Laboratory for Cancer Research, Frederick, Maryland, USA

^cCenter for Infectious Disease Imaging, Radiology and Imaging Sciences, Clinical Center, National Institutes of Health, Bethesda, Maryland, USA

^dEmerging Viral Pathogens Section, National Institute of Allergy and Infectious Diseases, National Institutes of Health, Frederick, Maryland, USA

ABSTRACT Marburg virus (MARV) is a highly virulent zoonotic filovirid that causes Marburg virus disease (MVD) in humans. The pathogenesis of MVD remains poorly understood, partially due to the low number of cases that can be studied, the absence of state-of-the-art medical equipment in areas where cases are reported, and limitations on the number of animals that can be safely used in experimental studies under maximum containment animal biosafety level 4 conditions. Medical imaging modalities, such as whole-body computed tomography (CT), may help to describe disease progression *in vivo*, potentially replacing ethically contentious and logistically challenging serial euthanasia studies. Towards this vision, we performed a pilot study, during which we acquired whole-body CT images of 6 rhesus monkeys before and 7 to 9 days after intramuscular MARV exposure. We identified imaging abnormalities in the liver, spleen, and axillary lymph nodes that corresponded to clinical, virological, and gross pathological hallmarks of MVD in this animal model. Quantitative image analysis indicated hepatomegaly with a significant reduction in organ density (indicating fatty infiltration of the liver), splenomegaly, and edema that corresponded with gross pathological and histopathological findings. Our results indicated that CT imaging could be used to verify and quantify typical MVD pathogenesis versus altered, diminished, or absent disease severity or progression in the presence of candidate medical countermeasures, thus possibly reducing the number of animals needed and eliminating serial euthanasia.

IMPORTANCE Marburg virus (MARV) is a highly virulent zoonotic filovirid that causes Marburg virus disease (MVD) in humans. Much is unknown about disease progression and, thus, prevention and treatment options are limited. Medical imaging modalities, such as whole-body computed tomography (CT), have the potential to improve understanding of MVD pathogenesis. Our study used CT to identify abnormalities in the liver, spleen, and axillary lymph nodes that corresponded to known clinical signs of MVD in this animal model. Our results indicated that CT imaging and analyses could be used to elucidate pathogenesis and possibly assess the efficacy of candidate treatments.

KEYWORDS Marburg virus, computed tomography, filovirus, medical imaging, viral pathogenesis

Marburg virus (MARV) and Ravn virus (RAVV) are zoonotic filovirids that cause Marburg virus disease (MVD) in humans. MVD is a rare acute infectious disease associated with an average case fatality rate of 81% (1, 2). Over the last 55 years, there have been 16 known outbreaks of MVD worldwide (499 MARV cases, including

Editor Alison Sinclair, University of Sussex

This is a work of the U.S. Government and is not subject to copyright protection in the United States. Foreign copyrights may apply. Address correspondence to Venkatesh Mani, venky.mani@nih.gov.

*Present address: Jennifer Sword, Office of Research Services, Division of Occupational Health and Safety, National Institutes of Health, Bethesda, Maryland, USA.

§Present address: Ji Hyun Lee, Radiology and Imaging Sciences, Clinical Center, National Institutes of Health, Bethesda, Maryland, USA.

◇Present address: Nina Aiosa, Grand Canyon University, Phoenix, Arizona, USA.

∞Present address: Joshua C. Johnson, Moderna Therapeutics, Infectious Disease Research, Cambridge, Massachusetts, USA.

‡Present address: Peter B. Jahrling (retired), Integrated Research Facility at Fort Detrick, Division of Clinical Research, National Institute of Allergy and Infectious Diseases, National Institutes of Health, Fort Detrick, Frederick, Maryland, USA.

#Present address: Reed F. Johnson, Laboratory of Viral Diseases, Division of Intramural Research, National Institute of Allergy and Infectious Diseases, National Institutes of Health, Bethesda, Maryland, USA.

¶Present address: Lisa E. Hensley, National Bio and Agro-Defense Facility, U.S. Department of Agriculture, Manhattan, Kansas, USA.

**Present address: Irwin M. Feuerstein, MedStar Medical Group Radiology, Columbia, Maryland, USA.

The authors declare no conflict of interest.

Received 31 August 2022

Accepted 1 February 2023

Published 10 April 2023

398 deaths; 3 RAVV cases, including 2 deaths). Almost all cases occurred in or originated from arid woodlands in eastern, central, and southern Africa, but recent individual cases in Equatorial Guinea, Ghana, and Guinea indicate an even broader distribution (1, 3–5). The only information on the clinical presentation of MVD comes from a few case reports from early outbreaks in West Germany and Yugoslavia (6–19), several individual case studies (20–27), and scant descriptions of more recent cases (28–30). Although these accounts suggest that the clinical presentation of MVD overlaps with more-well-characterized Ebola virus disease (31, 32), there are still major gaps in the understanding of disease transmission, natural history, and the host-pathogen determinants of severe disease and lethality. This information is crucial to help prevent and treat this severe condition beyond the supportive care measures used in outbreak settings.

Because of gaps in the description of MVD in humans, animal models have been necessarily leaned upon for characterizing MARV infection and disease and to evaluate the efficacy of virus-targeted or specific disease-targeted candidate medical countermeasures (MCMs). Nonhuman primates (NHPs) serve as the preferred animal model for MVD (2). Experimental exposure of crab-eating macaques and rhesus monkeys to MARV, usually by intramuscular inoculation, results in severe disease and almost uniform lethality, with clinicopathological features similar to human MVD (33, 34). Both models have been used to evaluate candidate MCMs (35–40), with small molecules (favipiravir [41], galidesivir [42], and remdesivir [43]) tested in crab-eating macaques and therapeutic antibodies tested in rhesus monkeys (44, 45). Most recently, combination therapy with a MARV-specific monoclonal antibody and remdesivir was able to rescue NHPs at 6 days after exposure (versus each therapeutic alone), providing an important proof of concept in this model (46).

However, studies of MVD (and filovirid diseases in general) in NHPs are hampered by significant financial, logistical, and safety challenges and are associated with ethical concerns (47). In addition, *in vivo* disease readouts of filovirus-exposed NHPs have been mainly limited to clinical assessments and clinical sample analyses. The evaluation of disease-specific and organ-specific pathophysiology has mostly been confined to *ex vivo* histopathological and ultrastructural investigations, with some studies examining viral titers, gene expression, evaluation of local immune processes, proteomics, and metabolomics. Such an approach is useful to establish the “ground truth” of organ damage, but it is expensive and labor-intensive, as in-depth characterization in a typical natural history study requires serial euthanasia of NHPs at different time points after virus exposure. Compelled by a desire to minimize the overall number of NHPs used, there is a need to develop and validate efficient noninvasive *in vivo* experimental tools to read out disease-related organ involvement and shed light on and address critical questions about MVD pathogenesis and assess the efficacy of candidate MCMs.

In many disciplines, including the study of infectious diseases, *in vivo* imaging is gaining interest as a tool to noninvasively monitor disease course and treatment efficacy in animal studies and human clinical trials (48–50). High-resolution computed tomography (CT) imaging, with or without injection of contrast media, can augment clinical, laboratory, and gross and histological pathology assessments during disease progression by providing quantitative readouts of organ morphology to identify and characterize structural and functional changes (such as texture, radiodensity, organ size, occurrence of focal lesions, and vascular perfusion). In the case of MVD, *in vivo* CT imaging may offer complementary information to standard clinical laboratory biomarkers (mainly of liver and/or kidney dysfunction) and could potentially replace gross and histological pathology (35, 37–39, 51, 52) at time points prior to the terminal time point, once data are appropriately bridged and established as cross-predictive.

In this study, we used whole-body CT imaging to investigate the temporal course of disease in MARV-exposed rhesus monkeys, with a focus on the liver and spleen, two key organs in the pathophysiology of MVD. We qualitatively and quantitatively compared imaging results to corresponding virological, biochemical, and gross and microscopic pathological findings. Our results indicated that CT imaging could be used in

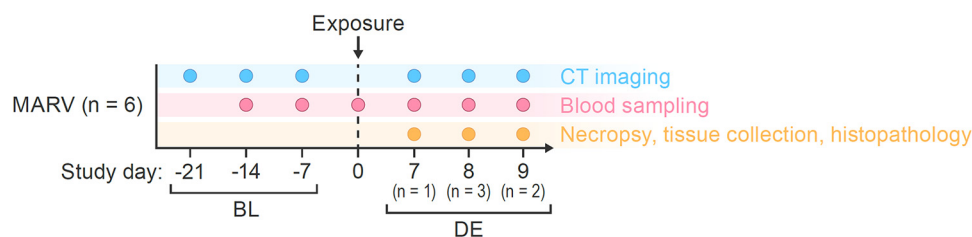


FIG 1 Study design. A total of 6 rhesus monkeys were imaged 21, 14, and 7 days prior to and on the day of euthanasia after MARV exposure. MARV, Marburg virus; CT, computed tomography; BL, baseline; DE, day of euthanasia.

the optimal future to verify and quantify typical MVD-specific organ changes that can be longitudinally measured and serve as proxy of histopathologic disease, enabling evaluation of natural history and of candidate MCMs without the need for serial euthanasia.

RESULTS

In this study, we conducted noninvasive *in vivo* medical imaging with CT to monitor qualitative and quantitative changes in organ structure in 6 rhesus monkeys exposed to MARV via intramuscular (i.m.) inoculation. CT imaging was performed 3 times before virus exposure (within 3, 2, and 1 week of exposure) to assess reliability of the imaging readouts at baseline. A fourth CT scan was performed on the day that animals met criteria for euthanasia (terminal day). (See Fig. 1 for an overview of the study design.) A total of 24 CT imaging sessions occurred during the entire study. As previously reported (53), before and after exposure (including at euthanasia), blood samples were drawn for virological and biochemical analyses and complete blood cell counts. After euthanasia, necropsies were performed, gross pathology was evaluated, and collected tissues were processed for histopathological analyses, including MARV immunohistochemistry (IHC) and *in situ* hybridization (ISH). Transmission electron microscopy of tissue samples was also performed.

Qualitative CT imaging findings. Qualitative analysis of non-contrast-enhanced CT imaging after MARV exposure revealed abnormalities in the liver, spleen, and axillary lymph nodes at the time of euthanasia. All monkeys had hepatomegaly, splenomegaly, and marked reduction in liver and spleen density (measured in Hounsfield units [HU]), compared to baseline scans. CT images also revealed enlargement of axillary lymph nodes ipsilateral to the brachium of virus inoculation with diffuse infiltration of axillary fat. Fat, expected to be present under normal circumstances within the axilla, was absent on the day of euthanasia in the axillary lymph nodes ipsilateral to the brachium where virus inoculation occurred. In all monkeys, the mean attenuation of the axillary lymph nodes ipsilateral to the brachium of virus inoculation increased on average ≈ 35 HU, and the mean attenuation of the axillary lymph nodes contralateral to the brachium of virus inoculation was ≈ 25 HU. This finding was consistent with those previously reported for filovirus infections in NHPs (54). While there were slight visual differences, in all monkeys, the volume of the axillary lymph nodes contralateral to the brachium of virus inoculation was not notably changed from the corresponding baseline volumes. In 5 of 6 monkeys, signs of moderate to severe hemorrhage and mild to severe lymphoid depletion were present in the axillary nodes ipsilateral to the brachium of virus inoculation. Moderate edema in the adjacent soft tissue was present in 2 of the monkeys, and signs indicative of possible lymphoid degeneration were present in 3 of the monkeys (Fig. 2A and B). In one monkey, CT imaging after MARV exposure revealed changes that appeared to be consistent with acute pancreatitis (Fig. 2C and D); in others, severe edema of the pancreas, ascites, abdominal distension, and mesenteric edema were observed. An overall summary of CT imaging findings on the day of euthanasia is presented in Table 1.

Quantitative CT imaging measurements. To quantify noninvasive disease readouts, we first analyzed organ volume and density data derived from CT imaging of the liver (Fig. 3) and spleen (Fig. 4). The absence of meaningful differences in volume or

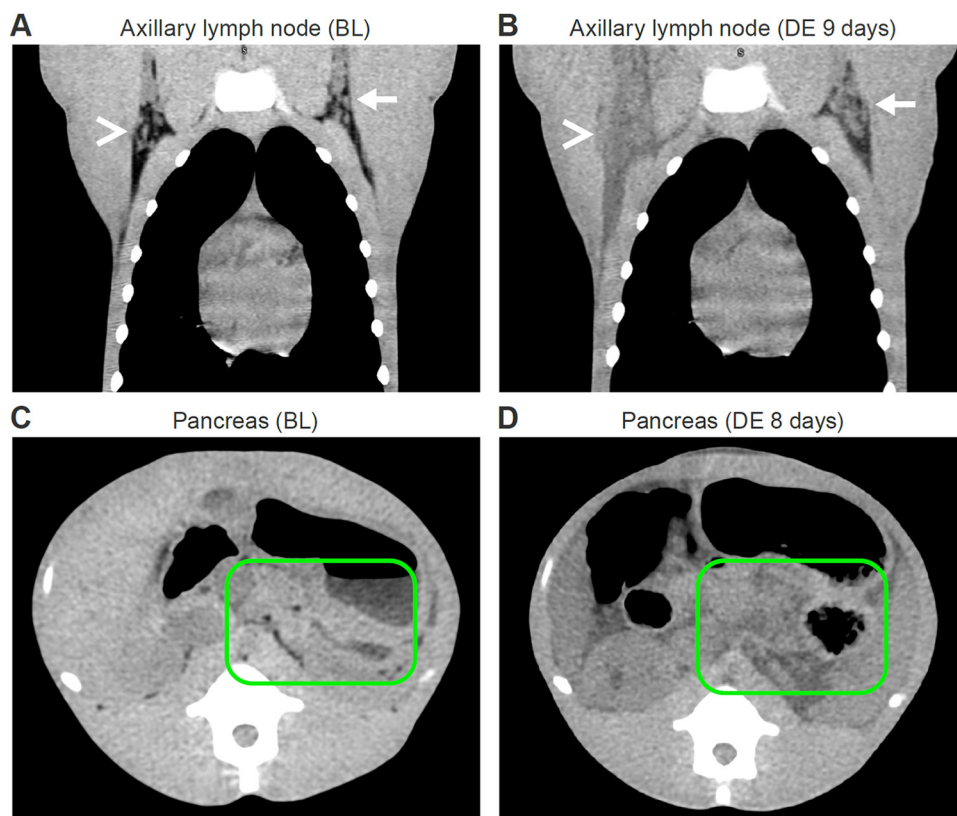


FIG 2 Qualitative CT imaging without contrast (rhesus monkey). (Top) Coronal view of bilateral axillary adenopathy after exposure to MARV via the intramuscular route. (A) Baseline scan shows normal axillary nodes bilaterally. (B) Scan on day of euthanasia, 9 days after exposure, shows right axillary adenopathy and diffuse infiltration of axillary fat (white arrowhead) and left axillary lymphadenopathy (white arrow). (Bottom) Axial views of changes in pancreas following MARV exposure. (C) Baseline scan shows normal pancreas (encircled with green line) and retroperitoneum. (D) Scan on day of euthanasia, 8 days after exposure, shows replacement of the area of the pancreas with low-radiodensity tissue (encircled with green line), which proved to be pancreatic exocrine atrophy at necropsy. BL, baseline; DE, day of euthanasia.

radiodensity across the 3 baseline images indicated reproducibility of the imaging method. Quantitative analysis revealed significant enlargement (hepatomegaly) (Fig. 3B) ($P < 0.001$) and decreased radiodensity (Fig. 3C) ($P < 0.001$) of the liver in MARV-exposed monkeys compared to baseline. Additionally, splenic enlargement (splenomegaly) (Fig. 4B) ($P < 0.001$) and decreased radiodensity (Fig. 4C) ($P < 0.001$) were observed on the day of euthanasia compared to baseline.

Hematology, serum chemistry, and assessment of viremia. Clinical chemistry, hematology, virology, and some focused pathology data from this study have been previously published (53). Notably, all MARV-exposed animals were highly viremic, as demonstrated in plasma by plaque assay and real-time reverse transcription PCR. Clinical chemistry abnormalities were consistent with those previously reported for MARV-exposed rhesus monkeys (38, 53, 55, 56), indicating reduced hepatic function and hepatocellular injury or necrosis. As in previous studies (38, 53, 55, 56), increased levels of several cytokines and chemokines were detected at terminal stages of disease in all animals. Concomitant imaging and serum chemistry data were available from the following time points: 2 weeks before exposure, 1 week before exposure, and on the day of euthanasia. Correlations of hematological and serum chemistry data with quantitative imaging measures (volume and radiodensity) of liver and spleen are shown in Fig. S1 to S4 in the supplemental material.

Pathology, IHC, and ISH. Gross pathological examination confirmed CT findings of hepatomegaly, along with fatty changes and focal small hemorrhages. Livers from all monkeys were enlarged, and fatty changes, comprised of a yellow color and greasy consistency,

TABLE 1 Summary of CT imaging findings on day of euthanasia in various organs

CT imaging finding(s)		Spleen	Kidney	Pancreas	Stomach and bowels	Axillary lymph nodes
Animal no., day of euthanasia	Liver	Gallbladder	Kidney	Pancreas	Stomach and bowels	Axillary lymph nodes
1, day 8	Hepatomegaly; hypodensity	Inferior enlargement	Mild enlargement	Unremarkable	Unremarkable	Enlargement of right axillary lymph node, infiltration of right axillary fat and extension to the right pectoralis muscle
2, day 8	Mild hepatomegaly; hypodensity	Loss of gallbladder shadow ^a ; high density	Enlarged in anterior posterior dimension	Unremarkable	Stomach and bowel distended	Lymphadenopathy; infiltration and edema of right axillary fat, extension of edema into right pectoralis muscle, surrounding subcutaneous tissue, and down the right chest wall
3, day 7	Hepatomegaly; hypodensity; loss of vascular conspicuity	Loss of gallbladder shadow ^a	Displaced by distended stomach	Unremarkable	Gastric distention; thickened colon; fluid in esophagus	Right axillary lymphadenopathy, infiltration of fat in right axilla
4, day 8	Hepatomegaly; hypodensity	High density in lumen; thickened wall	Mild enlargement	Focal low density; signs of pancreatitis	Mesenteric edema; ascites; thickened colon walls	Right axillary lymphadenopathy with infiltration of right axillary fat and fluid surrounding nodes; mild lymphadenopathy in left axilla
5, day 9	Hepatomegaly; hypodensity; marked enlargement of left hepatic lobe	Loss of gallbladder shadow ^a	Enlarged in anterior posterior dimension	Unremarkable	Unremarkable	Right axillary lymphadenopathy, infiltration and edema of right axillary fat, and extension of edema into right pectoralis muscle and surrounding subcutaneous tissue
6, day 9	Hepatomegaly; hypodensity	High density	Splenomegaly; hypodensity	Low density	Low density in retroperitoneum	Bilateral axillary adenopathy; infiltration of right axillary fat; edema

^aLoss of gallbladder shadow could also be indicative of decrease in liver radiodensity, causing a lack of separate visualization of gallbladder.

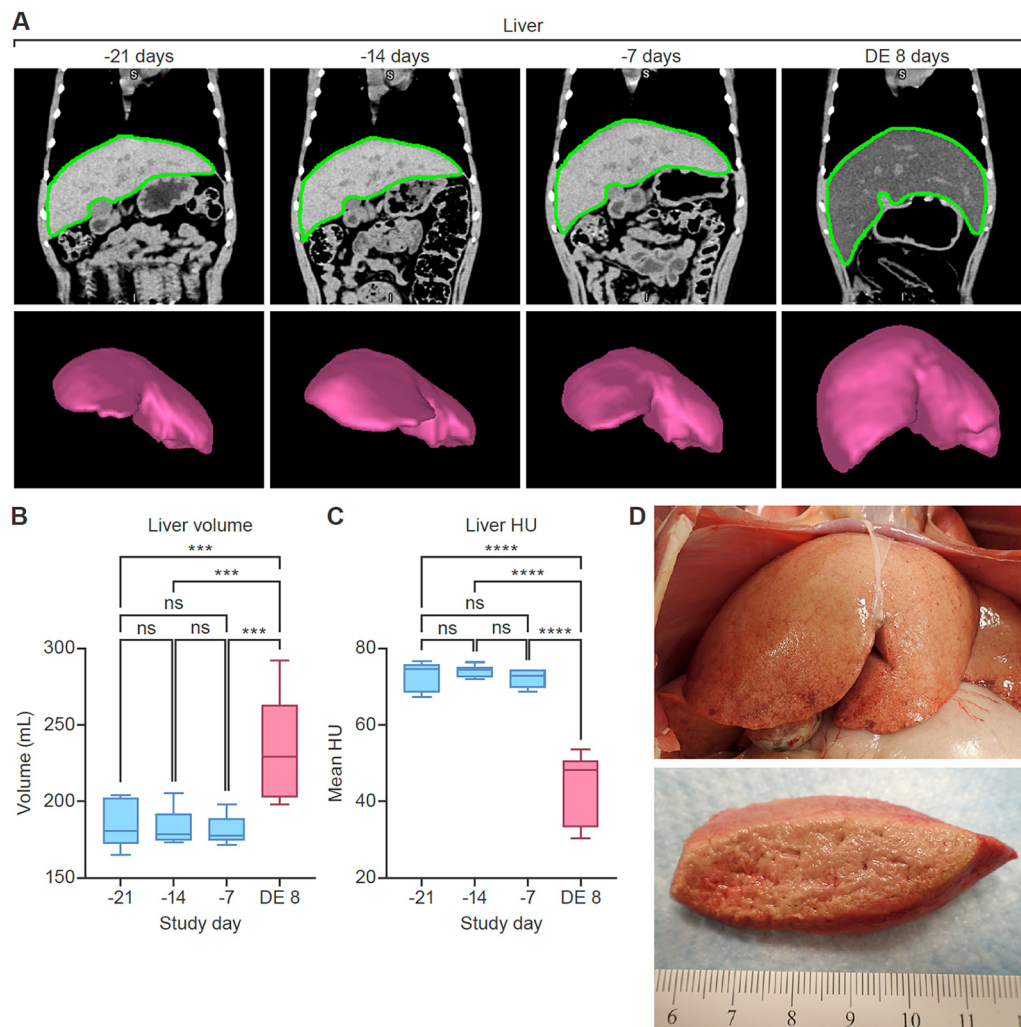


FIG 3 Quantitative CT imaging results (rhesus monkey liver). Comparison of baseline scans and those acquired on the day of euthanasia shows hepatomegaly and decreased radiodensity after MARV exposure. (A) Coronal CT images and 3D volume renderings of the liver, based on segmentation masks. Regions of interest segmenting the liver (green borders) were automatically generated using a machine-learning-based algorithm. Data from 3 baseline imaging sessions were highly reproducible. (B) Changes in liver volume. (C) Changes in liver radiodensity (expressed in Hounsfield units [HU]). (D) Gross pathology of the liver on the day of euthanasia. The liver was markedly enlarged, with rounded edges, pale tan-yellow color, and a greasy and friable consistency (lipidosis and necrosis). ns, not significant; DE, day of euthanasia (8 days postexposure).

were present in 5 of 6 animals. Major histopathological findings in the liver were hepatocellular vacuolization, degeneration, and necrosis (Fig. 5). Vacuolization was diffuse pan-acinar of the mild glycogen type or of the mild or mild-to-moderate macrovesicular or microvesicular lipid type. Minimal to mild hyperplasia in Kupffer cells was found in 5 of 6 livers (83.3%). The semiquantitative liver steatosis score for all monkeys was 3.0 ± 0.0 (mean \pm standard deviation) and consistent across all regions. Radiolucency of all livers (showing a similar reduction in density from baselines in all monkeys) was consistent with the liver steatosis scores.

Grossly, the spleen was either mildly (3 of 6) or moderately (3 of 6) enlarged in all MARV-exposed monkeys, with a friable consistency (consistent with necrosis) in all organs (Fig. 4); this finding was consistent with previous reports (38, 53, 55, 56). Splenic histopathology (Fig. S6A to C) was also consistent with previous reports (38, 55, 56). Overall, pathology findings corresponded to the mild or moderate splenomegaly and decreased radiodensity observed by CT imaging.

Consistent with previous studies (38, 53, 55, 56), MARV could be demonstrated in the

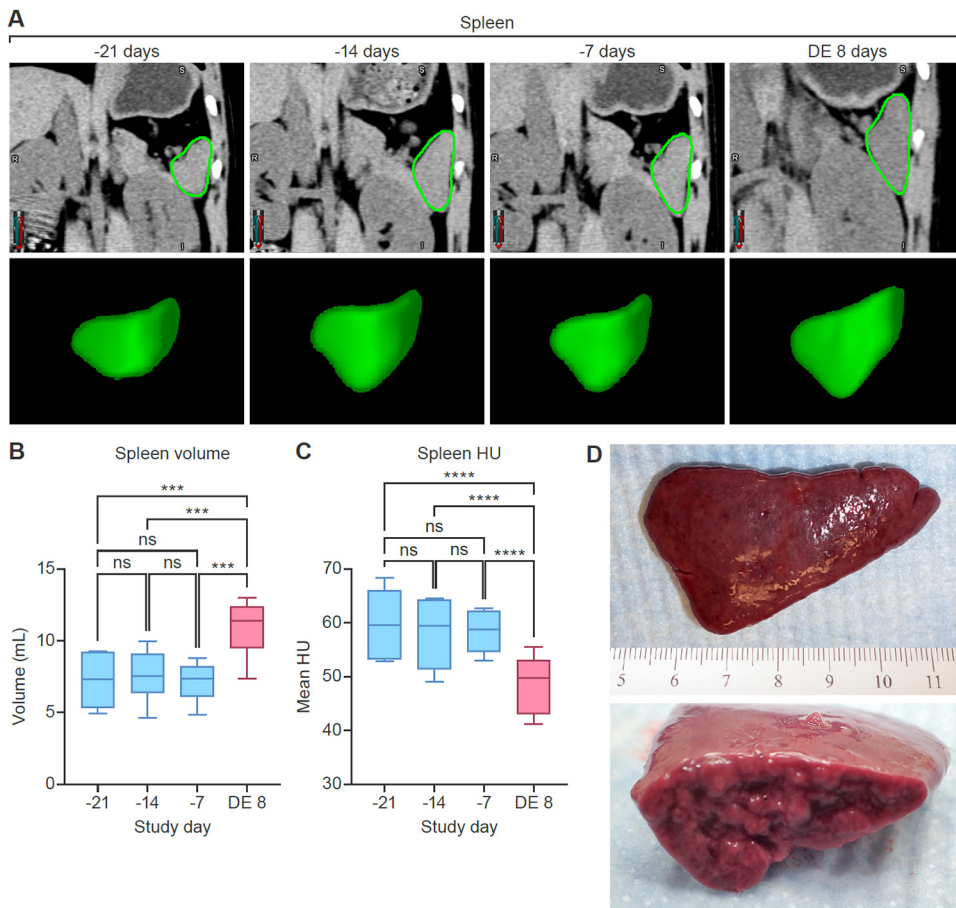


FIG 4 Quantitative CT imaging results (rhesus monkey spleen). Comparison of baseline scans and those acquired on the day of euthanasia shows splenomegaly and decreased radiodensity after MARV exposure. (A) Coronal CT images and 3D volume renderings of the spleen, based on segmentation masks. Regions of interest segmenting the spleen (green borders) were automatically generated using a machine-learning-based algorithm. Data from 3 baseline imaging sessions were highly reproducible. (B) Changes in spleen volume. (C) Changes in spleen radiodensity (expressed as Hounsfield units [HU]). (D) Gross pathology of the spleen on the day of euthanasia. The spleen was moderately enlarged, with rounded edges and a friable consistency. ns, not significant; DE, day of euthanasia (8 days postexposure).

liver and spleen. MARV was identified in hepatocytes and Kupffer cells by transmission electron microscopy (TEM), IHC, and ISH. IHC staining was particularly prominent in the splenic red pulp of all the animals.

In general, gross and histopathological characterization of axillary lymph nodes and surrounding tissues (Fig. S5D and E) supported CT findings. The degree of lymphadenopathy, infiltration of axillary fat, and edema observed by CT was consistent with the level of lymphocyte depletion and necrosis observed on histopathology. MARV infection was associated with significant lymphoid tissue abnormality, including necrosis of lymphoid follicles and medulla and widespread proliferation of reticuloendothelial tissue in the lymph nodes, all consistent with previous clinical reports (57). Histology of the exocrine pancreas showed diffuse and marked atrophy of the acinar cells with edema of the intervening stroma, and the drop in acini resulted in a condensation of the small ducts. The remaining acinar cells were small with loss of apical zymogen granules and vacuolation of the apical cytoplasm (Fig. S5F and G). However, no evidence of pancreatitis was found on histopathology in the animal that had signs of pancreatitis by CT imaging.

A summary of gross and histopathological findings from the livers and spleens of these animals is presented in Table S2.

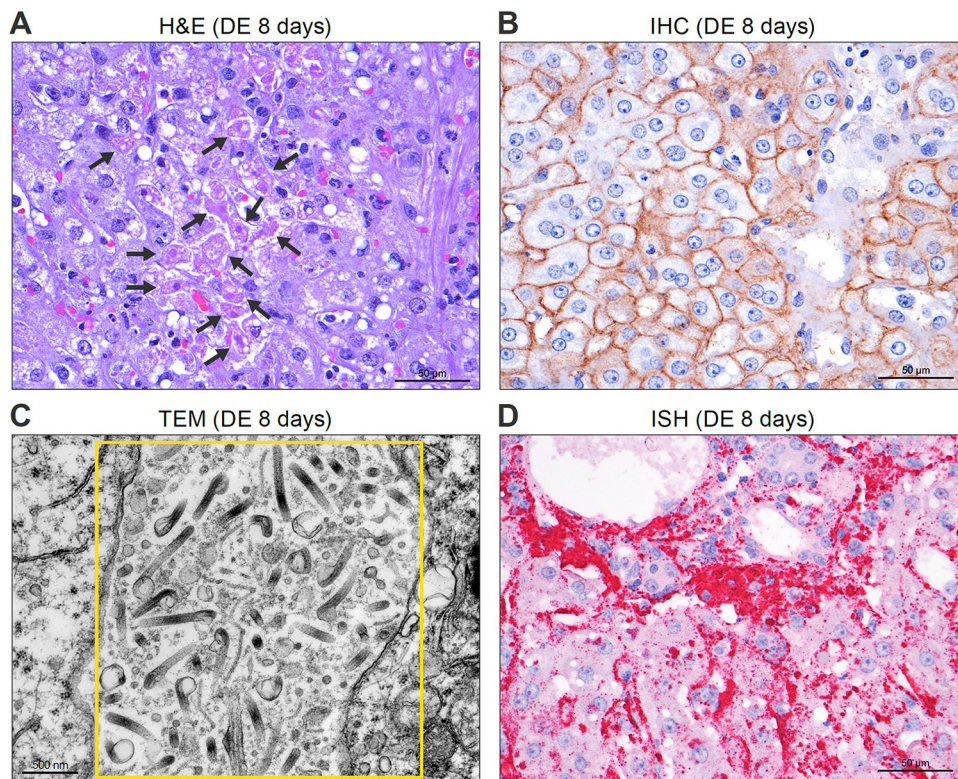


FIG 5 Liver histopathology images (rhesus monkey) on day of euthanasia (DE), 8 days after MARV exposure. (A) Tissue stained with hematoxylin and eosin (H&E) shows multifocal to coalescing hepatocellular degeneration and necrosis that affected approximately 20% of hepatocytes and diffuse mild to moderate microvesicular lipid-type cytoplasmic vacuolation of hepatocytes (black arrows). (B) IHC detection of MARV glycoprotein (brown) in hepatocytes, Kupffer cells, and sinusoids. (C) TEM showing abundant mature MARV particles (yellow box) between hepatocytes. (D) ISH results, demonstrates abundant MARV genome (darker pink) in viable and degenerate hepatocytes and Kupffer cells.

DISCUSSION

Multimodality imaging readouts can be leveraged to provide organ-level information on changes in morphology and function during the natural history of diseases caused by high-consequence pathogens, such as MVD, included here in an animal model of disease. Moreover, careful quantification of these imaging abnormalities ultimately enables correlation with already-benchmarked biomarkers of disease, such as with histopathology. Determining and validating these correlations in an appropriate animal model would provide a surrogate readout (of disease severity and organ damage) that might eliminate the need for serial euthanasia in large natural-history studies and also provide a “near-ground-truth” readout of disease, useful in the evaluation of therapeutic interventions.

In our study of MARV-exposed rhesus monkeys, comparison of baseline to terminal CT imaging revealed exposure-related abnormalities of liver, spleen, and axillary lymph nodes, with substantial changes in CT-derived liver and spleen volumes. CT imaging findings were supported by gross and microscopic pathology and consistent with those previously reported for MARV-exposed rhesus monkeys (38, 55, 56). In particular, terminal hepatomegaly and liver hypodensity changes shown on CT scans were in concordance with gross pathological and likely with underlying histopathologic findings (i.e., fatty vacuolation, hepatocellular necrosis, and edema of varied severities). These are also consistent with similar observations of patients in the clinical setting (58). Interestingly, the magnitude of change in imaging abnormalities paralleled the severity of disease observed by histologic or ultrastructural examination. Terminal CT abnormalities noted in these NHPs were considered consistent with diffuse hepatic injury, reflected in necrosis,

edema, increased vacuolization, and fat accumulation observed in (rare) histopathologic specimens from patients with fatal MVD. Draining axillary lymph node involvement ipsilateral to the inoculation site was ubiquitous and substantial in this model; regional lymphadenopathy was also similar to what has been described in humans (9, 17, 59).

While these proof-of-concept results are encouraging, we acknowledge several limitations, including the small number of subjects, the absence of “mid-disease” serial imaging between pre-exposure and terminal scanning, and lack of intravenous contrast in CT imaging. Regarding the number of animals and the imaging frequency, these data were obtained from an $n = 6$ confirmation-of-virulence study with a secondary goal of identifying viral distribution in particular immune-privileged (and other) terminal tissues of interest. This secondary goal of the base study was to potentially inform understanding of the pathophysiology of postacute sequelae, as observed in human survivors of MVD. For example, viral distribution and/or any associated pathological changes were specifically sought in these rhesus monkeys in the central and peripheral nervous system (e.g., peripheral nerves, autonomic ganglia), the eyes (e.g., the iris), and reproductive tissues (53). Toward both goals, the course of these (ultimately) lethal acute infections was intentionally as “uninterrupted” as possible to avoid interference in the natural history. By definition, imaging studies require the use of anesthesia for a substantial amount of time (for each scan), and it was decided that compressing multiple imaging time points into this confirmation of virulence study risked compromising those goals. Therefore, our study did not fully demonstrate the utility of longitudinal postexposure CT imaging in tracking organ changes in MVD.

Certainly, the limited proof of concept provided here argues for follow-up longitudinal studies that include more frequent serial CT imaging. This intended work would optimally serve to further map CT abnormalities to traditional disease markers, with particular interest in meaningfully correlating the noninvasive CT image proxy to histopathology, both at earlier stages of disease progression and at end of life.

Although imaging findings were largely consistent with findings obtained by evaluating biomarkers and histopathology, interpretation of the inconsistencies was also limited by small numbers. This was highlighted, for example, in an animal with CT imaging signs of pancreatitis for which serum amylase activity was not elevated, nor was there histopathologic evidence of pancreatitis. Instead, amylase activity markedly declined during the course of infection (with acinar cell atrophy by histology), consistent with inanition. More data are needed to determine whether inconsistencies (illustrated by this example) truly reflect uncoupling of imaging and biochemical and tissue signals (i.e., an inaccurate proxy versus differential sensitivities and specificities [unsurprising] or simply stochastic variability [also unsurprising]). The small sample size limits interpretation in these cases as well as the generalizability of even the consistent findings.

Finally, imaging was performed without intravenous CT contrast to avoid potential nephrotoxicity in the setting of volume depletion and prerenal azotemia (and to avoid altering the natural history). In future studies, intravenous contrast administration might be useful for identifying lesions that may be indiscernible on noncontrast CT.

Despite these limitations, our study underscores the potential value of noninvasive imaging for the characterization of organ involvement following exposure to high-consequence pathogens. The contribution of the magnitude and dynamic trajectory of liver and spleen dysfunction to the clinical course and outcomes in patients with MVD is yet to be clarified, as is the potential role of serial noninvasive proxies of disease severity to serve as meaningful surrogates in the evaluation of MCMs. Our study may be a proof-of-concept first step toward using CT (and other imaging modalities) to attain these goals in models of MVD. Coupling CT with other imaging modalities, such as positron emission tomography (PET) and/or magnetic resonance imaging (MRI), may enable the acquisition of multiparametric imaging data sets that can simultaneously probe interdependent disease processes in addition to organ volume and density. Examples are the imaging of inflammation with [^{18}F]FDG PET, specific

immune cell populations through appropriate immune-PET tracers, or organ-specific processes by tailored PET radiotracers or molecular MRI probes.

Our study proves that medical imaging can noninvasively capture MARV-associated disruption of homeostasis at the organ level in MARV-exposed rhesus monkeys, with focus on the liver, spleen, and draining lymph nodes. Although qualitative imaging readouts may be useful to crudely characterize disease, we also quantified liver and spleen volumes and radiodensity before and after MARV exposure; quantitative imaging readouts could be used as objective endpoints in evaluation of MCMs and/or in less-invasive natural-history studies that do not require serial euthanasia. It is hoped that the traction provided by disease-specific imaging markers serving as surrogate endpoints might not only reduce experimental burden (of NHPs in particular) but also lead to more rapid transition of novel candidate MCMs to improve outcomes at the clinical bedside.

In the clinical setting, a limited few case reports have demonstrated the utility of imaging to characterize disease during or just after the acute phase of a disease caused by high-consequence pathogens. For example, MRI has been used to document meningoencephalitis in patients with Ebola virus disease (60) and after Hendra virus infection (61) and Nipah virus infection (62–65). However, application of medical imaging during disease outbreaks remains largely unexplored. As therapeutic options improve and positively impact patient outcomes, imaging may become a useful tool for characterizing persistent syndromes in disease survivors that would be otherwise opaque to standard clinical and laboratory examinations.

MATERIALS AND METHODS

Experimental design. This study was performed at a maximum containment (biosafety level 4) facility (66, 67). (See Fig. 1 for an overview of the study design.) A total of 6 (2 male, 4 female) healthy adult rhesus monkeys (*Macaca mulatta* (Zimmermann, 1780)) of Chinese origin (Worldwide Primates, Miami, FL, USA), weighing 6.70 to 8.56 kg, were exposed via the i.m. route in the brachium with a target dose of 1,000 PFU of Marburg virus/H.sapiens-tc/AGO/2005/Ang-1379v (BioSample identifier [SAMN05916381](#); referred to here as MARV). Exposure dose was confirmed as approximately 856 PFU by means of a 2.5% Avicel 591 (RC-591 NF, FMC Biopolymer) plaque assay method described previously (68). Blood was sampled and serum was collected for biomarkers and viral load determination at baseline, on several days over the course of disease progression, and on the day of euthanasia (Fig. 1). Monkeys were CT imaged in a unique maximum-containment suite (67, 69, 70) 3 times before exposure to assess variability over time (3, 2, and 1 week prior to inoculation) and on the day of euthanasia. Criteria for euthanasia for the animals used in this study have been previously reported (53). Time of euthanasia varied at day 7 ($n = 1$), day 8 ($n = 3$), and day 9 ($n = 2$). Gross necropsy was performed after euthanasia, followed by routine tissue fixation, embedding, sectioning, staining, and imaging for histology. MARV IHC, ISH, and electron microscopy were also performed following previously published protocols (53).

CT imaging acquisition. For CT imaging, each monkey was anesthetized with ketamine (15 mg/kg of body weight, i.m.), intubated, and maintained on a ventilator using isoflurane (2 to 2.5%) inhalation, and placed on the scanner bed in a supine head-out feet-in position. Monkeys were monitored for the duration of anesthesia. Three sets of baseline images were obtained 3, 2, and 1 week prior to MARV exposure; the final scan (on the day of euthanasia) was acquired when a monkey reached endpoint criteria (7 to 9 days postexposure). Images were obtained using a Philips Precedence 16 CT scanner (Philips Healthcare, Cleveland, OH, USA) without contrast, and monkeys underwent a 45- to 50-s breath hold during acquisition. All monkeys underwent whole-body CT imaging in the transaxial plane. Images were acquired in helical scan mode with the following parameter settings: 140 kVp, 250 mAs per slice, 1-mm thickness, 0.5-mm increments, 0.688-mm pitch, collimation of 16×0.75 , and rotation time of 0.5 s. Images were reconstructed to isotropic 1-mm³ voxels using an iterative reconstruction with B (soft tissue) and D (bone and lung) filters.

CT imaging analyses. (i) Qualitative analyses. For all animals, CT images acquired at baseline (3 sets) and on the day of euthanasia were examined for qualitative assessments, and findings were recorded using MIM software version 6.7 (MIM Software, Cleveland, OH, USA). While the entire chest and abdomen of the animal was visualized, the liver, spleen, and axillary lymph nodes were specifically examined for CT characteristics.

(ii) Quantitative analyses. Quantitative analyses of images acquired at baseline (3 sets) and on the day of euthanasia focused on the liver and spleen. Whole liver and spleen volumes, as well as corresponding radiodensity values (in HU), were obtained in a semiautomated fashion using manual correction of automated liver and spleen contours, obtained using a previously described machine-learning-based segmentation algorithm (71). The algorithm training parameters, loss function, and postprocessing steps for liver segmentation were performed as previously described (71) and applied to spleen segmentation.

Briefly, input patches were extracted randomly from an equal number of spleen and nonspleen regions. As the spleen is comparatively a much smaller organ than the liver, the input patch size was

heuristically set to $128 \times 128 \times 16$. Similar to liver segmentation, a 10-fold cross-validation of 80 scans from 32 monkeys was performed, and the method was found effective for spleen segmentation, with an average 90% Dice score, a statistic used to gauge the similarity of 2 samples, in our case the performance of image segmentation models (72).

Liver and spleen segmentation masks were exported to MIM software version 7.1, and errors in segmentation were corrected. Using the corrected segmentations, volume, and radiodensity, information was automatically computed. Additionally, a region-growing algorithm was used to segment the volume of axillary lymph nodes (73), and radiodensities of the segmented volumes of axillary lymph nodes ipsilateral and contralateral to the virus injection site were recorded.

Hematology, serum chemistry, and assessment of viremia. Hematological assessments were performed on whole blood using an XT-2000iV analyzer (Sysmex America, Lincolnshire, IL, USA). Serum chemistries were measured with Piccolo General Chemistry 13 panels (Abaxis, Union City, CA, USA) on samples collected prior to and after exposure to MARV. Serum chemistries were determined using methods previously published (53). Results were correlated with liver and spleen densities and quantitatively obtained organ volumes. MARV titers in plasma were determined by plaque assay using grivet (*Chlorocebus aethiops* (Linnaeus, 1758)) kidney epithelial Vero E6 cells and by measuring MARV genome equivalents using real-time reverse transcription PCR, both as previously described (53).

Necropsy, tissue processing, pathology, IHC, and ISH. Monkeys were euthanized in accordance with previously defined experimental endpoints (74), based on their clinical condition; complete necropsies were conducted. All tissues were fixed, inactivated, sectioned, processed, and examined for routine histology, as previously described (53, 75). IHC, ISH with the RNAscope 2.5 HD RED kit (Advanced Cell Diagnostics), and TEM were performed according to methods previously described (53). Additionally, a semiquantitative liver steatosis scoring system was adapted from a previously published method (76). Briefly, steatosis was graded on a scale of 0 to 3 for samples in 4 liver locations (pancinar, azonal, zone 1, and zone 3), and an average was assigned as the score for each liver.

Statistical analyses. To determine changes in CT imaging readouts after MARV exposure, a one-way analysis of variance (ANOVA) was used to compare the volumes and radiodensities of livers and spleens across the 4 imaging time points (3 baseline days and day of euthanasia) for each monkey. A Tukey posttest was used to compare differences between each time point.

Pearson's correlations of blood biochemistry measures, of liver and spleen densities, and of organ volumes across all time points were characterized by matching clinical chemistry and imaging data (i.e., at -2 weeks, -1 week, and day of euthanasia). A paired Student's *t* test was performed with averaged baseline and day of euthanasia radiodensity of axillary lymph nodes. Two-tailed tests were used, and *P* values of <0.05 were considered statistically significant. Statistical analyses were performed in Prism version 9.3 (GraphPad Software, San Diego, CA, USA).

Ethics approval. NHPs were housed in a facility accredited by the Association for Assessment and Accreditation of Laboratory Animal Care International. The animal study protocol was approved by the National Institutes of Health, National Institute of Allergy and Infectious Diseases, Division of Clinical Research, Animal Care and Use Committee. Experiments were performed in compliance with the U.S. Department of Agriculture Animal Welfare Act regulations, the National Research Council's *Guide for the Care and Use of Laboratory Animals* (77), Public Health Service policy, and the NIH Animal Research Advisory Committee guidelines.

SUPPLEMENTAL MATERIAL

Supplemental material is available online only.

SUPPLEMENTAL FILE 1, PDF file, 3.7 MB.

ACKNOWLEDGMENTS

We thank David X. Liu and Donna L. Perry for performing gross necropsies and tissue collections; John B. Bernbaum, Randall Hart, and Amanda Hischak for performing transmission electron microscopy, immunohistochemistry, and *in situ* hybridization, respectively; and Ricky Adams and Tracey Burdette for performing plaque assays and real-time reverse transcription PCR assays. We thank Anya Crane for critically editing the manuscript and Jiro Wada for figure preparation. (All of these personnel are affiliated with the National Institutes of Health (NIH), National Institute of Allergy and Infectious Diseases (NIAID), Division of Clinical Research, Integrated Research Facility at Fort Detrick).

This research was supported in part through the NIH NIAID prime contract with Battelle Memorial Institute (HHSN2722007000161) and, subsequently, contracts with Laulima Government Solutions, LLC (HHSN272201800013C) and Kelly Services (75N93019D00027). J.C.J. performed this work as an employee of Battelle Memorial Institute. M.A.C., J. Sword, C.B., and K.C. performed this work as employees of Laulima Government Solutions, LLC. J.H.L., C.C., and J.H.K. performed this work as employees of Tunnell Government Services, a subcontractor of Battelle Memorial Institute and Laulima Government Solutions (contracts

HHSN2722007000161 and HHSN272201800013C, respectively). V.M. performed this work as an employee of Kelly Services (under contract number 75N93019D00027 with NIAID task order 75N93021F00010). This work was also supported in part with federal funds from the NIH National Cancer Institute (NCI), under contract 75N910D00024 with Leidos Biomedical Research, Inc. I.C. and J. Solomon performed this work as employees of Leidos Biomedical Research, Inc., supported by the Clinical Monitoring Research Program Directorate, Frederick National Lab for Cancer Research, sponsored by NCI. This project has been also partially funded by the NIH Clinical Center Radiology and Imaging Sciences Center for Infectious Disease Imaging (S.M.S.R. and W.C.). This work was also supported in part by the NIH NIAID Division of Intramural Research.

The funders had no role in study design, data collection and interpretation, or the decision to submit the work for publication. The views and conclusions contained in this document are those of the authors and should not be interpreted as necessarily representing the official policies, either expressed or implied, of the U.S. Department of Health and Human Services or of the institutions and companies affiliated with the authors, nor does mention of trade names, commercial products, or organizations does not imply endorsement by the U.S. Government.

We declare no conflict of interest.

REFERENCES

- Kuhn JH, Crozier I. 2022. Ebolavirus and marburgvirus infections, p 1645–1652. In Loscalzo J, Fauci AS, Kasper DL, Hauser SL, Longo DL, Jameson JL (ed), *Harrison's Principles of Internal Medicine*, 21st ed, vol 2. McGraw-Hill Education, Columbus, Ohio, USA.
- Kuhn JH, Amarasinghe GK, Perry DL. 2020. *Filoviridae*, p 449–503. In Howley PM, Knipe DM, Whelan SPJ (ed), *Fields Virology*, 7th ed., vol 1 (Emerging viruses). Lippincott Williams & Wilkins, Philadelphia, PA, USA.
- Koundouno FR, Kafetzopoulou LE, Faye M, Renevey A, Soropogui B, Ifono K, Nelson EV, Kamano AA, Tolno C, Annibaldis G, Millimono SL, Camara J, Kourouma K, Doré A, Millimouno TE, Tolno FMB, Hinzmann J, Soubrier H, Hinrichs M, Thielebein A, Herzer G, Pahlmann M, Ki-Zerbo GA, Formenty P, Legand A, Wiley MR, Faye O, Diagne MM, Sall AA, Lemey P, Bah A, Günther S, Keita S, Duraaffour S, Magassouba N. 2022. Detection of Marburg virus disease in Guinea. *N Engl J Med* 386:2528–2530. <https://doi.org/10.1056/NEJM2120183>.
- World Health Organization. 2022. Ghana declares first-ever outbreak of Marburg virus disease. <https://www.afro.who.int/countries/ghana/news/ghana-declares-first-ever-outbreak-marburg-virus-disease-0>.
- ProMED. 2023. Marburg virus disease - Equatorial Guinea (01): (KIE-NTEM) WHO confirmed. Archive Number: 20230214.8708367. <https://promedmail.org/promed-post/?id=8708367>.
- Baltzer G, Slenczka W, Stöppler L, Schmidt-Wilke HA, Hermann E, Siegert R, Martini GA. 1979. Marburg-Virus-Krankheit. Verlaufsbeobachtungen über 12 Jahre (1967–1979), p 1203–1206. In Schlegel B (ed), *Verhandlungen der Deutschen Gesellschaft für Innere Medizin*. J. F. Bergmann Verlag, Munich, Germany.
- Bechtelsheimer H, Jacob H, Solcher H. 1968. Zur Neuropathologie der durch grüne Meerkatzen (*Cercopithecus aethiops*) übertragenen Infektionskrankheiten in Marburg. *Dtsch Med Wochenschr* 93:602–604. <https://doi.org/10.1055/s-0028-1105102>.
- Egbring R, Slenczka W, Baltzer G. 1971. Clinical manifestations and mechanisms of the haemorrhagic diathesis in Marburg virus disease, p 41–49. In Martini GA, Siegert R (ed), *Marburg virus disease*. Springer-Verlag, Berlin, Germany.
- Gedigk P, Bechtelsheimer H, Korb G. 1968. Die pathologische Anatomie der "Marburg-Virus"-Krankheit (sog. "Marburger Affenkrankheit"). *Dtsch Med Wochenschr* 93:590–601. <https://doi.org/10.1055/s-0028-1105101>.
- Gedigk P, Bechtelsheimer H, Korb G. 1971. Pathologic anatomy of the Marburg virus disease, p 50–53. In Martini GA, Siegert R (ed), *Marburg virus disease*. Springer-Verlag, Berlin, Germany.
- Gedigk P, Korb G, Bechtelsheimer H. 1968. Die pathologische Anatomie der "Marburg-Virus"-Krankheit, p 317–322. In Seifert G (ed), *Verhandlungen der Deutschen Gesellschaft für Pathologie*, vol 52. Gustav Fischer Verlag, Stuttgart, Germany.
- Helm EB. 1978. Klinik der Marburg-Virus-Infektion. *MMW Münch Med Wochenschr* 120:1563–1564.
- Jacob H. 1971. The neuropathology of the Marburg disease, p 54–61. In Martini GA, Siegert R (ed), *Marburg virus disease*. Springer-Verlag, Berlin, Germany.
- Jacob H, Solcher H. 1968. Über eine durch Meerkatzen (*Cercopithecus aethiops*) übertragene, zu Gliaknötchenencephalitis führende Infektionskrankheit ("Marburger Krankheit"). *Acta Neuropathol* 11:29–44. <https://doi.org/10.1007/BF00692793>.
- Korb G, Bechtelsheimer H, Gedigk P. 1968. Die wichtigsten histologischen Befunde bei der "Marburg-Virus"-Krankheit. *Dtsch Arztebl* 65:1089–1096.
- Martini GA. 1968. Klinik der Erkrankung durch das "Marburg-Virus" beim Menschen. *Med Welt* 19:1542.
- Martini GA. 1971. Marburg virus disease: clinical syndrome, p 1–9. In Martini GA, Siegert R (ed), *Marburg virus disease*. Springer-Verlag, Berlin, Germany.
- Ristanović ES, Kokoškov NS, Crozier I, Kuhn JH, Gligić AS. 2020. A forgotten episode of Marburg virus disease: Belgrade, Yugoslavia, 1967. *Microbiol Mol Biol Rev* 84:e00095-19. <https://doi.org/10.1128/MMBR.00095-19>.
- Stille W, Böhle E. 1971. Clinical course and prognosis of Marburg virus ("green monkey") disease, p 10–18. In Martini GA, Siegert R (ed), *Marburg virus disease*. Springer-Verlag, Berlin, Germany.
- Gear JHS. 1975. Marburg fever in the Johannesburg General Hospital. A personal account of the outbreak. *Bacteria* 1975:7–14.
- Gear JHS. 1989. Clinical aspects of African viral hemorrhagic fevers. *Rev Infect Dis* 11(Suppl 4):S777–S782. https://doi.org/10.1093/clinids/11.Supplement_4.S777.
- Gear JSS, Cassel GA, Gear AJ, Trappler B, Clausen L, Meyers AM, Kew MC, Bothwell TH, Sher R, Miller GB, Schneider J, Koornhof HJ, Gomperts ED, Isaacson M, Gear JHS. 1975. Outbreak of Marburg virus disease in Johannesburg. *Br Med J* 4:489–493. <https://doi.org/10.1136/bmj.4.5995.489>.
- Kuming BS, Kokoris N. 1977. Uveal involvement in Marburg virus disease. *Br J Ophthalmol* 61:265–266. <https://doi.org/10.1136/bjo.61.4.265>.
- Rippey JJ, Schepers NJ, Gear JHS. 1984. The pathology of Marburg virus disease. *S Afr Med J* 66:50–54.
- Smith DH, Isaacson M, Johnson KM, Bagshawe A, Johnson BK, Swanepoel R, Killey M, Siogok T, Koinange Keruga W. 1982. Marburg-virus disease in Kenya. *Lancet* 319:816–820. [https://doi.org/10.1016/S0140-6736\(82\)91871-2](https://doi.org/10.1016/S0140-6736(82)91871-2).
- van Paassen J, Bauer MP, Arbous MS, Visser LG, Schmidt-Chanasit J, Schilling S, Ölschläger S, Rieger T, Emmerich P, Schmetz C, van de Berkortel F, van Hoek B, van Burgel ND, Osterhaus AD, Vossen ACTM, Günther S, van Dissel JT. 2012. Acute liver failure, multiorgan failure, cerebral oedema, and activation of proangiogenic and antiangiogenic factors in a case of Marburg haemorrhagic fever. *Lancet Infect Dis* 12:635–642. [https://doi.org/10.1016/S1473-3099\(12\)70018-X](https://doi.org/10.1016/S1473-3099(12)70018-X).
- Никифоров ВВ, Туровский ЮИ, Калинин ПП, Акинфеева ЛА, Каткова ЛР, Бармин ВС, Рябчикова ЕИ, Попкова НИ, Шестопалов АМ, Назаров ВП, Ведишев СВ, Нетесов СВ. 1994. Случай лабораторного заражения

- лихорадкой Марбург. *Ж Микробиол Эпидемиол Иммунобиол* 3: 104–106.
28. Bausch DG, Nichol ST, Muyembe-Tamfum JJ, Borchert M, Rollin PE, Sleurs H, Campbell P, Tshioke FK, Roth C, Colebunders R, Pirard P, Mardel S, Olinda LA, Zeller H, Tshomba A, Kulidri A, Libande ML, Mulangu S, Formenty P, Grein T, Leirs H, Braack L, Ksiazek T, Zaki S, Bowen MD, Smit SB, Leman PA, Burt FJ, Kemp A, Swanepoel R, International Scientific and Technical Committee for Marburg Hemorrhagic Fever Control in the Democratic Republic of the Congo. 2006. Marburg hemorrhagic fever associated with multiple genetic lineages of virus. *N Engl J Med* 355: 909–919. <https://doi.org/10.1056/NEJMoa051465>.
 29. Borchert M, Muyembe-Tamfum JJ, Colebunders R, Libande M, Sabue M, Van Der Stuyft P. 2002. Short communication: a cluster of Marburg virus disease involving an infant. *Trop Med Int Health* 7:902–906. <https://doi.org/10.1046/j.1365-3156.2002.00945.x>.
 30. Tshomba OA. 2005. Prédiction clinique de fièvre hémorragique de Marburg dans l'épidémie de Watsa. MS thesis. Prince Leopold Institute of Tropical Medicine, Antwerp, Belgium.
 31. Jacob ST, Crozier I, Fischer WA, Hewlett A, Kraft CS, Vega M-AdL, Soka MJ, Wahl V, Griffiths A, Bollinger L, Kuhn JH. 2020. Ebola virus disease. *Nat Rev Dis Primers* 6:13. <https://doi.org/10.1038/s41572-020-0147-3>.
 32. Feldmann H, Sprecher A, Geisbert TW. 2020. Ebola. *N Engl J Med* 382: 1832–1842. <https://doi.org/10.1056/NEJMra1901594>.
 33. Shifflett K, Marzi A. 2019. Marburg virus pathogenesis: differences and similarities in humans and animal models. *Virology* 16:165. <https://doi.org/10.1186/s12985-019-1272-z>.
 34. Siragam V, Siragam V, Wong G, Qiu X-G. 2018. Animal models for filovirus infections. *Zool Res* 39:15–24. <https://doi.org/10.24272/j.issn.2095-8137.2017.053>.
 35. Dye JM, Herbert AS, Kuehne AI, Barth JF, Muhammad MA, Zak SE, Ortiz RA, Prugar LI, Pratt WD. 2012. Postexposure antibody prophylaxis protects nonhuman primates from filovirus disease. *Proc Natl Acad Sci U S A* 109:5034–5039. <https://doi.org/10.1073/pnas.1200409109>.
 36. Smith LM, Hensley LE, Geisbert TW, Johnson J, Stossel A, Honko A, Yen JY, Geisbert J, Paragas J, Fritz E, Olinger G, Young HA, Rubins KH, Karp CL. 2013. Interferon- β therapy prolongs survival in rhesus macaque models of Ebola and Marburg hemorrhagic fever. *J Infect Dis* 208:310–318. <https://doi.org/10.1093/infdis/jis921>.
 37. Thi EP, Mire CE, Ursic-Bedoya R, Geisbert JB, Lee ACH, Agans KN, Robbins M, Deer DJ, Fenton KA, MacLachlan I, Geisbert TW. 2014. Marburg virus infection in nonhuman primates: therapeutic treatment by lipid-encapsulated siRNA. *Sci Transl Med* 6:250ra116. <https://doi.org/10.1126/scitranslmed.3009706>.
 38. Geisbert TW, Daddario-DiCaprio KM, Geisbert JB, Young HA, Formenty P, Fritz EA, Larsen T, Hensley LE. 2007. Marburg virus Angola infection of rhesus macaques: pathogenesis and treatment with recombinant nematode anticoagulant protein C2. *J Infect Dis* 196(Suppl 2):S372–S381. <https://doi.org/10.1086/520608>.
 39. Daddario-DiCaprio KM, Geisbert TW, Ströher U, Geisbert JB, Grolla A, Fritz EA, Fernando L, Kagan E, Jahrling PB, Hensley LE, Jones SM, Feldmann H. 2006. Postexposure protection against Marburg haemorrhagic fever with recombinant vesicular stomatitis virus vectors in non-human primates: an efficacy assessment. *Lancet* 367:1399–1404. [https://doi.org/10.1016/S0140-6736\(06\)68546-2](https://doi.org/10.1016/S0140-6736(06)68546-2).
 40. Cross RW, Mire CE, Feldmann H, Geisbert TW. 2018. Post-exposure treatments for Ebola and Marburg virus infections. *Nat Rev Drug Discov* 17: 413–434. <https://doi.org/10.1038/nrd.2017.251>.
 41. Bixler SL, Bocan TM, Wells J, Wetzel KS, Van Tongeren SA, Dong L, Garza NL, Donnelly G, Cazares LH, Nuss J, Soloveva V, Koistinen KA, Welch L, Epstein C, Liang L-F, Giesing D, Lenk R, Bavari S, Warren TK. 2018. Efficacy of favipiravir (T-705) in nonhuman primates infected with Ebola virus or Marburg virus. *Antiviral Res* 151:97–104. <https://doi.org/10.1016/j.antiviral.2017.12.021>.
 42. Warren TK, Wells J, Panchal RG, Stuthman KS, Garza NL, Van Tongeren SA, Dong L, Retterer CJ, Eaton BP, Pegoraro G, Honnold S, Bantia S, Kotian P, Chen X, Taubenheim BR, Welch LS, Minning DM, Babu YS, Sheridan WP, Bavari S. 2014. Protection against filovirus diseases by a novel broad-spectrum nucleoside analogue BCX4430. *Nature* 508:402–405. <https://doi.org/10.1038/nature13027>.
 43. Porter DP, Weidner JM, Gomba L, Bannister R, Blair C, Jordan R, Wells J, Wetzel K, Garza N, Van Tongeren S, Donnelly G, Steffens J, Moreau A, Bearss J, Lee E, Bavari S, Cihlar T, Warren TK. 2020. Remdesivir (GS-5734) is efficacious in cynomolgus macaques infected with Marburg virus. *J Infect Dis* 222:1894–1901. <https://doi.org/10.1093/infdis/jiaa290>.
 44. Mire CE, Geisbert JB, Borisevich V, Fenton KA, Agans KN, Flyak AI, Deer DJ, Steinkellner H, Bohorov O, Bohorova N, Goodman C, Hiatt A, Kim DH, Pauly MH, Velasco J, Whaley KJ, Crowe JE, Jr, Zeitlin L, Geisbert TW. 2017. Therapeutic treatment of Marburg and Ravn virus infection in nonhuman primates with a human monoclonal antibody. *Sci Transl Med* 9:eaa18711. <https://doi.org/10.1126/scitranslmed.aai8711>.
 45. Brannan JM, He S, Howell KA, Prugar LI, Zhu W, Vu H, Shulenin S, Kailasan S, Raina H, Wong G, Rahim MN, Banadyga L, Tierney K, Zhao X, Li Y, Holtsberg FW, Dye JM, Qiu X, Aman MJ. 2019. Post-exposure immunotherapy for two ebolaviruses and Marburg virus in nonhuman primates. *Nat Commun* 10:105. <https://doi.org/10.1038/s41467-018-08040-w>.
 46. Cross RW, Bornholdt ZA, Prasad AN, Borisevich V, Agans KN, Deer DJ, Abelson DM, Kim DH, Shestowsky WS, Campbell LA, Bunyan E, Geisbert JB, Fenton KA, Zeitlin L, Porter DP, Geisbert TW. 2021. Combination therapy protects macaques against advanced Marburg virus disease. *Nat Commun* 12:1891. <https://doi.org/10.1038/s41467-021-22132-0>.
 47. Carvalho C, Gaspar A, Knight A, Vicente L. 2018. Ethical and scientific pitfalls concerning laboratory research with non-human primates, and possible solutions. *Animals (Basel)* 9:12. <https://doi.org/10.3390/ani9010012>.
 48. Fayad ZA, Mani V, Woodward M, Kallend D, Abt M, Burgess T, Fuster V, Ballantyne CM, Stein EA, Tardif JC, Rudd JH, Farkouh ME, Tawakol A, Dal PI, dal-PLAQUE Investigators. 2011. Safety and efficacy of dalcetrapib on atherosclerotic disease using novel non-invasive multimodality imaging (dal-PLAQUE): a randomised clinical trial. *Lancet* 378:1547–1559. [https://doi.org/10.1016/S0140-6736\(11\)61383-4](https://doi.org/10.1016/S0140-6736(11)61383-4).
 49. Cardoso AC, Figueiredo-Mendes C, Villela-Nogueira CA, Marcellin P. 2022. Staging fibrosis in chronic viral hepatitis. *Viruses* 14:660. <https://doi.org/10.3390/v14040660>.
 50. Nooreldeen R, Bach H. 2021. Current and future development in lung cancer diagnosis. *Int J Mol Sci* 22:8661. <https://doi.org/10.3390/ijms22168661>.
 51. Warren TK, Warfield KL, Wells J, Swenson DL, Donner KS, Van Tongeren SA, Garza NL, Dong L, Mourich DV, Crumley S, Nichols DK, Iversen PL, Bavari S. 2010. Advanced antisense therapies for postexposure protection against lethal filovirus infections. *Nat Med* 16:991–994. <https://doi.org/10.1038/nm.2202>.
 52. Geisbert TW, Hensley LE, Geisbert JB, Leung A, Johnson JC, Grolla A, Feldmann H. 2010. Postexposure treatment of Marburg virus infection. *Emerg Infect Dis* 16:1119–1122. <https://doi.org/10.3201/eid1607.100159>.
 53. Cooper TK, Sword J, Johnson JC, Bonilla A, Hart R, Liu DX, Bernbaum JG, Cooper K, Jahrling PB, Hensley LE. 2018. New insights into Marburg virus disease pathogenesis in the rhesus macaque model. *J Infect Dis* 218 (Suppl 5):S423–S433. <https://doi.org/10.1093/infdis/jiy367>.
 54. Castro MA, Solomon J, Lee JH, Sayre PJ, Bartos C, Thomasson D, Bollinger L, Sword J, Hensley L, Johnson RF, Feuerstein IM. 2021. Quantification of axillary lymphadenopathy from CT images of filovirus infections in non-human primates: sensitivity and evaluation of radiomics-based methods, abstr 13117. *Proc SPIE Medical Imaging 2020* <https://doi.org/10.1117/12.2548627>.
 55. Haas R, Maass G, Oehlert W. 1969. Disease in laboratory personnel associated with vervet monkeys. 3. Experimental infections of monkeys, p 138–139. *In* Goldsmith EI, Moor-Jankowski J (ed), *Using primates in medical research, part II, recent comparative research, 1969/01/01 ed*, vol 3. S. Karger, Basel, Switzerland.
 56. Johnston SC, Lin KL, Twenhafel NA, Raymond JL, Shamblin JD, Wollen SE, Wlazlowski CB, Wilkinson ER, Botto MA, Goff AJ. 2015. Dose response of MARV/Angola infection in cynomolgus macaques following IM or aerosol exposure. *PLoS One* 10:e0138843. <https://doi.org/10.1371/journal.pone.0138843>.
 57. Mehedi M, Groseth A, Feldmann H, Ebihara H. 2011. Clinical aspects of Marburg hemorrhagic fever. *Fut Virol* 6:1091–1106. <https://doi.org/10.2217/fvl.11.79>.
 58. Bechtelsheimer H, Korb G, Gedigk P. 1972. The morphology and pathogenesis of "Marburg virus" hepatitis. *Hum Pathol* 3:255–264. [https://doi.org/10.1016/S0046-8177\(72\)80079-0](https://doi.org/10.1016/S0046-8177(72)80079-0).
 59. Havemann K, Schmidt HA. 1971. Haematological findings in Marburg virus disease: evidence for involvement of the immunological system, p 34–40. *In* Martini GA, Siegert R (ed), *Marburg virus disease*. Springer-Verlag, Berlin, Germany.
 60. Chertow DS, Nath A, Suffredini AF, Danner RL, Reich DS, Bishop RJ, Childs RW, Arai AE, Palmore TN, Lane HC, Fauci AS, Davey RT. 2016. Severe meningoencephalitis in a case of Ebola virus disease: a case report. *Ann Intern Med* 165:301–304. <https://doi.org/10.7326/M15-3066>.
 61. Nakka P, Amos GJ, Saad N, Jeavons S. 2012. MRI findings in acute Hendra virus meningoencephalitis. *Clin Radiol* 67:420–428. <https://doi.org/10.1016/j.crad.2011.10.008>.

62. Anam AM, Ahmad J, Huq SMR, Rabbani R. 2019. Nipah virus encephalitis: MRI findings. *J R Coll Physicians Edinb* 49:227–228. <https://doi.org/10.4997/jrcpe.2019.312>.
63. Sarji SA, Abdullah BJ, Goh KJ, Tan CT, Wong KT. 2000. MR imaging features of Nipah encephalitis. *AJR Am J Roentgenol* 175:437–442. <https://doi.org/10.2214/ajr.175.2.1750437>.
64. Lim CC, Sitoh YY, Lee KE, Kurup A, Hui F. 1999. Meningoencephalitis caused by a novel paramyxovirus: an advanced MRI case report in an emerging disease. *Singapore Med J* 40:356–358.
65. Lim CC, Sitoh YY, Hui F, Lee KE, Ang BS, Lim E, Lim WE, Oh HM, Tambyah PA, Wong JS, Tan CB, Chee TS. 2000. Nipah viral encephalitis or Japanese encephalitis? MR findings in a new zoonotic disease. *AJNR Am J Neuroradiol* 21:455–461.
66. de Kok-Mercado F, Kutlak FM, Jahrling PB. 2011. The NIAID Integrated Research Facility at Fort Detrick. *Appl Biosaf* 16:58–66. <https://doi.org/10.1177/153567601101600202>.
67. Jahrling PB, Keith L, St Claire M, Johnson RF, Bollinger L, Lackemeyer MG, Hensley LE, Kindrachuk J, Kuhn JH. 2014. The NIAID Integrated Research Facility at Frederick, Maryland: a unique international resource to facilitate medical countermeasure development for BSL-4 pathogens. *Pathog Dis* 71:213–218. <https://doi.org/10.1111/2049-632X.12171>.
68. Honko AN, Johnson JC, Marchand JS, Huzella L, Adams RD, Oberlander N, Torzewski LM, Bennett RS, Hensley LE, Jahrling PB, Olinger GG. 2017. High dose sertraline monotherapy fails to protect rhesus macaques from lethal challenge with Ebola virus Makona. *Sci Rep* 7:5886. <https://doi.org/10.1038/s41598-017-06179-y>.
69. Byrum R, Keith L, Bartos C, St Claire M, Lackemeyer MG, Holbrook MR, Janosko K, Barr J, Pustl D, Bollinger L, Wada J, Coe L, Hensley LE, Jahrling PB, Kuhn JH, Lentz MR. 2016. Safety precautions and operating procedures in an (A)BSL-4 laboratory. 4. Medical imaging procedures. *J Vis Exp* <https://doi.org/10.3791/53601>.
70. Lackemeyer MG, Kok-Mercado F, Wada J, Bollinger L, Kindrachuk J, Wahl-Jensen V, Kuhn JH, Jahrling PB. 2014. ABSL-4 aerobiology biosafety and technology at the NIH/NIAID Integrated Research Facility at Fort Detrick. *Viruses* 6:137–150. <https://doi.org/10.3390/v6010137>.
71. Reza SMS, Bradley D, Aiosa N, Castro M, Lee JH, Lee B-Y, Bennett RS, Hensley LE, Cong Y, Johnson R, Hammoud D, Feuerstein I, Solomon J. 2021. Deep learning for automated liver segmentation to aid in the study of infectious diseases in nonhuman primates. *Acad Radiol* 28(Suppl 1): S37–S44. <https://doi.org/10.1016/j.acra.2020.08.023>.
72. Dice LR. 1945. Measures of the amount of ecologic association between species. *Ecology* 26:297–302. <https://doi.org/10.2307/1932409>.
73. Pham DL, Xu C, Prince JL. 2000. Current methods in medical image segmentation. *Annu Rev Biomed Eng* 2:315–337. <https://doi.org/10.1146/annurev.bioeng.2.1.315>.
74. Warren TK, Trefry JC, Marko ST, Chance TB, Wells JB, Pratt WD, Johnson JC, Mucker EM, Norris SL, Chappell M, Dye JM, Honko AN. 2014. Euthanasia assessment in Ebola virus infected nonhuman primates. *Viruses* 6: 4666–4682. <https://doi.org/10.3390/v6114666>.
75. Cooper TK, Huzella L, Johnson JC, Rojas O, Yellayi S, Sun MG, Bavari S, Bonilla A, Hart R, Jahrling PB, Kuhn JH, Zeng X. 2018. Histology, immunohistochemistry, and in situ hybridization reveal overlooked Ebola virus target tissues in the Ebola virus disease guinea pig model. *Sci Rep* 8:1250. <https://doi.org/10.1038/s41598-018-19638-x>.
76. Kleiner DE, Brunt EM, Van Natta M, Behling C, Contos MJ, Cummings OW, Ferrell LD, Liu Y-C, Torbenson MS, Unalp-Arida A, Yeh M, McCullough AJ, Sanyal AJ, Nonalcoholic Steatohepatitis Clinical Research Network. 2005. Design and validation of a histological scoring system for nonalcoholic fatty liver disease. *Hepatology* 41:1313–1321. <https://doi.org/10.1002/hep.20701>.
77. National Research Council. 2011. Guide for the care and use of laboratory animals. National Academy of Sciences, Washington, DC.